

Full Length Article

Pressure effects on soot formation in turbulent CH₄ flames in an O₂/CO₂ atmosphere

Muhammad Bukar ^a, Suman Basnet ^a, Taesung Kim ^b, William L. Roberts ^a, Gaetano Magnotti ^{a,c,*}

^a Physical Science and Engineering Division, Clean Combustion Research Centre, King Abdullah University of Science and Technology, Thuwal 23955, Saudi Arabia

^b IEFE Distributed Thermal Energy Systems, ZHAW School of Engineering, Technikumstrasse 9, 8400 Winterthur, Switzerland

^c INSA Rouen-Normandie, CNRS UMR6614-CORIA, Saint'Etienne du Rouvray 76801, France

ARTICLE INFO

Keywords:
Oxy-fuel combustion
Carbon dioxide
Soot volume fraction
Methane

ABSTRACT

This study investigates the effect of pressure on soot formation in turbulent oxy-fuel methane jet flames using Planar Laser-Induced Incandescence (PLII) calibrated using Light Extinction Measurements (LEM). The bulk jet velocity was held constant while the pressure was increased from 1 bar ($Re = 3500$) to 3 bar ($Re = 10,600$) and 5 bar ($Re = 17,700$) inside our new high-pressure vessel. DSLR imaging revealed increased flame luminosity and reduced flame length with rising pressure, consistent with previous literature. Planar soot volume fraction (SVF) measurements showed a significant increase in soot levels with pressure, with the maximum mean SVF increasing by factors of 7 and 14 at 3 bar and 5 bar, respectively. The intermittency analysis indicated a more continuous soot field at elevated pressures, while the Probability Density Function (PDF) analysis demonstrated a shift toward higher soot concentrations with reduced variability. Radially and volumetrically integrated SVF further confirmed a pressure dependence, with total soot loading (volume-integrated SVF) showing a $P^{2.1}$ pressure dependence. However, when normalized by the fuel mass flow rate, this dependence weakens to show almost linear behavior, suggesting that both pressure and additional carbon input contribute to the observed trends. These findings provide new insights into the pressure-driven mechanisms governing soot formation in high-pressure turbulent oxy-fuel flames and provide dataset for validating numerical models.

1. Introduction

Curbing CO₂ emissions has been a major objective of industries and governments due to its contribution to global warming in the past several decades. Carbon Capture and Storage (CCS) [1] is one of the principal technologies employed to mitigate CO₂ emissions' environmental impact. These technologies can be broadly categorized into pre-combustion, post-combustion, and oxy-combustion technologies [2]. As the name implies, pre-combustion technologies involve removing CO₂ before combustion occurs. This is achieved by converting the fuel into a mixture of H₂ and CO through processes such as steam-methane reforming [3]. The CO₂ is then removed from the flue gas, leaving pure H₂ to be burned instead. The post-combustion method involves scrubbing the CO₂ from the flue gas after combustion in air takes place. The problem with both these methods is that they increase the cost of electricity over conventional power plants by amounts ranging from 33 % to 64 % [4].

One of the most promising technologies for capturing CO₂ is oxy-fuel combustion. It involves burning fuel in oxygen obtained from an Air Separation Unit (ASU) at high pressures. In oxy-fuel combustion, a portion of the flue gas, especially CO₂, is used as a diluent to control the flame temperature. This combustion strategy eliminates concerns about NOx production, as no nitrogen is present when using nitrogen-free fuels. Several oxy-combustion-based power cycles have been proposed over the years, with the Semi-closed Oxy-Combustion Combined Cycle (SCOC-CC) [5] and the NET power Allam cycle [6] leading the race in terms of expected efficiency. Both of the aforementioned technologies require turbulent combustion at elevated pressures in O₂/CO₂ atmospheres. One of the main drawbacks of using oxy-combustion is the efficiency loss incurred in the production of pure O₂ in the ASU [7]. It is estimated that ASU's power consumption can exceed 15 % of the total power generation [8].

Soot is widely acknowledged as a major driver of climate change [9] and a significant threat to human health [10,11]. Thus, a proper understanding of soot formation at high pressures in O₂/CO₂

* Corresponding author at: INSA Rouen Normandie, CNRS UMR 6614-CORIA, Saint'Etienne du Rouvray, 76801, France.
E-mail address: gaetano.magnotti@coria.fr (G. Magnotti).

Nomenclature

| | |
|--------------------|------------------------------------------|
| SVF | Soot Volume Fraction |
| PLII | Planar Laser-Induced Incandescence |
| RMS | Root Mean Square |
| HAB (or x) | Height above burner |
| x/L _f | axial height normalized by flame height |
| PDF | Probability Density Function |
| SVF _{rad} | Radially Integrated Soot Volume Fraction |
| SVF _{vol} | Volume Integrated Soot Volume Fraction |

environments—approaching conditions similar to those in industrial oxy-combustion processes—is essential for minimizing the environmental impact of this technology.

When studying soot at high pressure, a decision has to be made as to whether the pressure would be increased while keeping velocities or the reactant flow rates constant [12]. Each of these decisions comes with distinct implications. Increasing pressure at constant flow rates leads to a decrease in velocities, making the flame appear more laminar at higher pressures [13]. Increasing pressure while maintaining velocities leads to an increase in the flow rates and also the Reynolds number. The high Reynolds number helps prevent the artificial “laminarisation” at high pressures, making comparisons between different conditions easier. Additionally, higher Reynolds numbers also increase turbulence–chemistry interaction, which influences soot inception and growth, as highlighted by Mahmoud et al. [14]. Hence, the Reynolds number and pressure effects are not independent and must be interpreted carefully.

Most high-pressure studies of soot in diffusion flames have been carried out at laminar conditions while the mass flow rates are kept constant [15–20]. Generally, these studies show a power law (CP^n) dependence of the mean maximum soot volume fraction or soot yield. For instance, Thompson et al. [15], using Spectral Emission Technique (SSE), found a P^2 dependence of maximum soot concentration in laminar methane diffusion flame burned in air between pressure ranges of 5–20 bar and $P^{1.2}$ for $P = 20$ –40 bar. Using the LII technique, McCain and Roberts [19] found that peak soot volume fraction scales with pressure as $P^{1.2}$ for methane-air and $P^{1.7}$ for ethylene-air flame for a pressure range of 1–15 bar and 1–16 bar, respectively.

Soot studies in turbulent flames have been scarce due to the inherent difficulty of running high-power turbulent flames in an enclosed environment. The earliest known study was by Flower [21], who used laser extinction measurements to examine the integrated soot volume fraction in turbulent ethylene–air flame at multiple axial locations. The pressures range from 1 bar to 8 bar. The study reports a pressure dependence of peak integrated soot volume fraction of $P^{1.4}$ up to 5 bar for the cases when the flame Reynolds number and characteristic residence time were held constant while varying the pressure. Subsequently, Fischer et al. [22] reported the influence of operating pressure on soot volume fraction and radiative heat transfer of kerosene spray flames. Their results showed a linear relation between soot and pressure in the 1–13 bar range.

More recently, Boyette et al. [12] used LII to investigate the effect of pressure on soot in turbulent ethylene–nitrogen jet flames in air coflow between 1–5 bar pressure range. In one series, they held the jet Reynolds number constant as pressure was increased from 1 bar to 5 bar, while in another, they fixed the reactant velocities constant. Both series' results showed that the peak mean soot volume fraction scaled with pressure with an exponent of 2.2 ($P^{2.2}$). Many of the abovementioned flames are part of the International Sooting Flames (ISF) workshop [23], a collaborative endeavor to foster collaboration between modelers and experimentalists by working on common target flames to improve the predictive capabilities of the modeling community.

All previous turbulent high-pressure soot studies have focused exclusively on air flames, leaving conditions in O₂/CO₂ mixtures largely unexplored. Yet such data are critical for developing and validating combustion models as well as improving our understanding of pressure effects on soot under oxy-fuel conditions.

The present study addresses this gap by providing the first quantitative soot measurements in high pressure turbulent jet oxy-methane flames in an environment of O₂/CO₂ = 50/50. Planar Laser-induced Incandescence (PLII), calibrated by light-extinction measurements, was used to provide information on soot volume fraction. DSLR images were also taken to provide further information on the topology of the examined flames.

2. Experimental techniques and setup

2.1. High pressure vessel.

The experiments were conducted inside our recently commissioned high-pressure vessel [13] to study oxy-fuel turbulent jet flames. The schematic of the setup is shown in Fig. 1, while the actual picture of the setup can be found in Fig. S1 of the supplementary material. The 1-meter-tall vessel core is made up of class 600,316 stainless steel pipe with a 10-inch inner diameter. The top flange of the vessel is equipped with an Equilibar back-pressure regulator (BPR) to maintain the pressure inside the vessel. The BPR is controlled by an electronic pressure regulator integrated into LabVIEW-controlled National Instruments hardware. A K-type thermocouple is inserted just before the BPR to read the temperature of the gases entering the BPR. The maximum allowable temperature of the BPR is 300 °C; however, we operated it below 250 °C to minimize the risk of damaging its diaphragm. As oxy-fuel flames generally have high flame temperatures, we continuously supply air to charge the vessel. The cooling air is obtained from a Mini-Verticus III compressor and enters from the bottom flange, flowing upward along the vessel walls, thereby diluting and cooling the hot flue gases before they reach the BPR. Once the flue gas temperature (mixed with the cooling air) approaches 250 °C at the inlet of the BPR, the LabVIEW was programmed to automatically shut the fuel flow into the vessel so as to avoid BPR malfunction.

The upper flange is fitted with a pressure relief valve to prevent pressure overshoots and ensure overall operational safety. On the bottom flange, we placed a pressure gauge and pressure transducer to check real-time pressure inside the vessel at all times, both visually and electronically, via the LabVIEW interface.

Two 1-inch and one 5-inch Raytek sight windows, located on the side flanges of the vessel, provide optical access. These sapphire windows have high IR transmissivity (>90 %) and withstand temperatures up to 200 °C. The large window is used for flame visualization and data collection, while the two smaller windows, located 90 degrees to it, are for laser sheet delivery and laser ignition, respectively. Laser ignition was achieved by placing a C-coated plano-convex spherical lens ($f = +100$ mm) inside the vessel. This lens is held by four guiding rods and a lens-holding cage system attached to the inner part of the flange. The lens focuses the laser beam at roughly the center of the burner inside, causing an ignition-inducing spark. The sight window through which the laser sheet entered the vessel was heated to 75 °C using heating tapes to prevent condensation, which was observed at higher pressures. Such condensation can absorb a significant portion of the 1064 nm laser energy, thereby reducing the LII signal; heating the window eliminated this effect.

2.2. Burner and flame conditions

The oxy-fuel burner consists of a round 1.75 mm CH₄ jet surrounded by a coflow stream with a 40 mm by 40 mm square cross-section. The coflow honeycomb is enclosed in a quartz window with a height of 289 mm. More details on the burner can be found in our previous study [24].

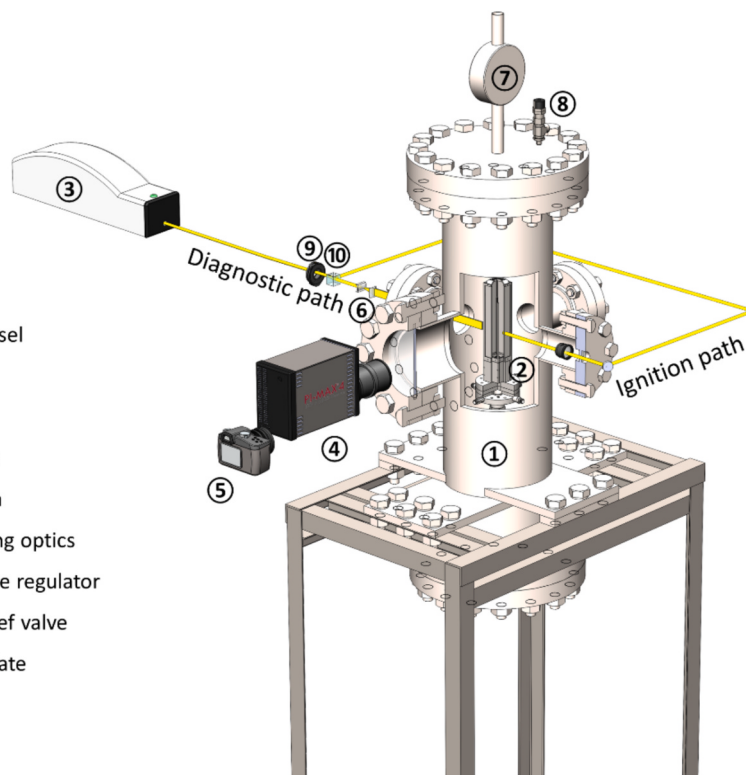


Fig. 1. Experimental setup for high-pressure LII measurements.

The burner was mounted on top of an X-Y-Z linear translation system to facilitate fine movement. The X-Y stage was primarily to align the burner to the laser sheet placed inside the vessel, while the Z-stage (with a 40 mm range) allows for scanning various portions of the flame. We were limited to this short-range Z-stage because we could not find larger-range stages that fit inside the vessel. This meant that we had to open the vessel and manually change the height of the Thorlabs post to scan the other sections of the flame. All gas flow rates were regulated using Bronkhorst mass flow controllers (MFCs), which were calibrated with a DryCal flow calibrator, ensuring a calibration accuracy of approximately $\pm 3\%$. The MFCs operated between 2 % and 90 % of their full-scale capacity and were controlled via LabVIEW.

Table 1 shows the test conditions used in this study. The fuel for all cases was a jet of methane with a velocity of 35 m/s, and the coflow was an O₂/CO₂ mixture with a molar composition of 50/50 and a velocity of 0.4 m/s. The ratio of jet velocity to coflow velocity is 87.5 for all cases. Increasing the O₂/CO₂ ratio reduces the flame length [24] and increases the lift-off velocity, countering the known effect of pressure in reducing the lift-off limit [13]. Furthermore, a 50/50 ratio of O₂/CO₂ ensures stable flames over the range of pressures and limits the flame height to below the burner window's height, preventing interaction with the chamber airflow. As soot formation peaks at about 40 % oxygen concentration for this burner [24], a 50 % O₂ content prevents excessively high soot loading that would make soot measurement inside the vessel difficult. The baseline case is a 3 kW turbulent flame at 1 bar with a bulk jet Reynolds number of ~ 3500 . The other two cases at 3 bar and 5 bar

were obtained by increasing the pressure while keeping the fuel and coflow velocities constant. The bulk jet velocities were held constant to ensure that the turbulence level approached more realistic conditions as pressure increased. The Reynolds number scaled with the pressure reaching a maximum value of $\sim 17,700$ at 5 bar. For flame series at constant velocities, the heat released scales linearly with the pressure, quickly reaching the maximum allowed exit temperature of the back-pressure regulator. Radiation heating increases the temperature of the vessel, and many damage the translation stage and the lenses placed inside. Increasing the cooling airflow absorbs the heat more rapidly and increases the maximum operating pressure, but reduces the run-time as the air accumulated in the tank by the compressor is quickly depleted. For this series of experiment, we limited measurements up to 5 bar.

2.3. Laser-Induced Incandescence (LII)

Soot volume fraction measurements were carried out using the Planar Laser-Induced Incandescence (PLII) technique calibrated by the Light Extinction Method (LEM). The fundamental output (1064 nm) of a Quantel Brilliant-B laser with a 10-Hz repetition rate and 5 ns pulse width was used. The 9 mm laser beam was split into two using a half-wave plate and a polarizer. The $\frac{1}{2}$ wave plate was used to adjust the percentage of the laser energy delivered to either the transmission side or the reflected side while the laser ran continuously at its maximum energy of 650 mJ. The reflected beam was raised with the help of a periscope and passed through a plano-concave cylindrical lens ($f = -100$ mm) and a plano-convex spherical lens ($f = +750$ mm) to form a ~ 67 mm tall laser sheet. This laser sheet's 20 mm more uniform central portion was sent through the vessel and into the burner to heat the soot particles. A 160 mJ laser energy (fluence of 0.25 J/cm^2), $\sim 50\%$ higher than the energy at the onset of the plateau region, was chosen to increase the robustness of the measurements to spatial and temporal laser fluence fluctuations. The curves for peak and integrated LII intensity at different laser fluences are shown in Fig. S2 of the supplementary material.

The transmitted laser beam was directed to the flange opposite the

Table 1
Flame conditions for our three turbulent oxy-fuel flames.

| Pressure (bar) | Re (–) | U_f (m/ s) | U_{ox} (m/ s) | Power (kW) | O ₂ / CO ₂ (–) | CH ₄ (L/ min) | O ₂ + CO ₂ (L/min) |
|-------------------|-----------|--------------------|-----------------------|---------------|--------------------------------------------|--------------------------------|---------------------------------------------|
| 1.0 | 3500 | 35 | 0.4 | 3 | 50/50 | 4.61 | 34.78 |
| 3.0 | 10,600 | 35 | 0.4 | 9 | 50/50 | 13.83 | 104.32 |
| 5.0 | 17,700 | 35 | 0.4 | 15 | 50/50 | 23.03 | 173.86 |

one used for laser sheet delivery mirrors and a periscope. This beam was then focused at the center of the burner by the +100 mm spherical lens mentioned in section 2.1. Once the flame is ignited, however, the transmission path is blocked by a beam dump, while the reflected path is used for diagnostic purposes.

LII signal was collected using an Intensified PI MAX 4 CCD camera optimized for visible range signal collection. The camera was equipped with a bandpass filter of 435 ± 40 nm, and the electronic gate had a delay of 50 ns and a width of 50 ns. This camera configuration was chosen in order to maximize LII signal. A Nikon lens (AF-S Micro Nikkor 105 mm 1:2.8) was mounted on the camera. For each condition, 700 images were acquired at a camera gain of 80 (arbitrary units) as a compromise between optimal SNR and dynamic range. For each flame condition, the average of two hundred single-shot images, taken with the laser blocked, provides the background. This averaged background was then subtracted from each of the 700 single shots to remove the average contribution of the flame luminosity. The uncertainty associated with background fluctuations corresponds to $\pm 3.19 \times 10^{-3}$, $\pm 9.17 \times 10^{-3}$, and $\pm 4.6 \times 10^{-2}$ for 1 bar, 3 bar, and 5 bar flames, respectively.

LEM was used to convert the LII intensity to soot volume fraction. A He-Ne laser ($\lambda = 633$ nm) was used to perform the extinction measurements, assuming soot absorption function $E(m) = 0.37$ [12]. The calibration flame and procedure found in [24] are the same as those used our 1 bar case. To minimize signal trapping effects, extinction-based calibration was performed separately at each pressure condition [12]. Uncertainty due to background subtraction and LEM calibration was estimated as $\pm 10\%$ combined, consistent with literature ranges [25].

3. Results and discussions

Fig. 2 shows the DSLR images of the three turbulent jet flames

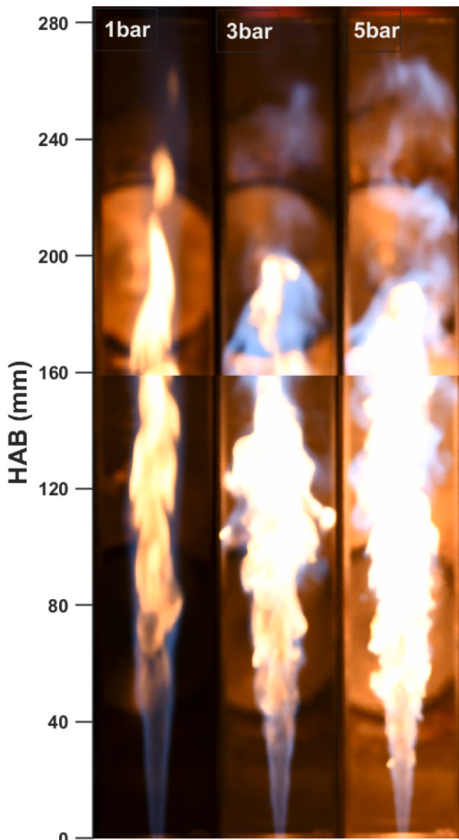


Fig. 2. DSLR images of the test cases mentioned in Table 1.

examined in this study. The images were taken at an identical camera setting of f/2.8, ISO 800, and a shutter speed of 1/1000 s. Due to the limitation of the vessel sight window, each flame image was obtained at two axial locations and then stitched together in post-processing. The figure shows increased luminosity as pressure increases from 1 bar to 5 bar, which agrees with Darabkhani et al. [26], who found average luminosity to increase with pressure up to 6 bar for methane diffusion flames. The 1 bar flame is the longest, comprising a blue premixed region at the base(arising from CH* chemiluminescence [27,28]) and a yellow luminous sooting part in the downstream locations. According to the classical turbulent flame length scaling by Delichatsios [29,30], the turbulent jet flame height decreases as pressure (and hence density) rises. This trend is evident here: the 5-bar flame is significantly shorter than the 1-bar flame, although the 3-bar and 5-bar flame lengths are quite similar.

3.1. Soot volume fraction distributions

The planar distribution of the mean, Root Mean Square (RMS), and instantaneous soot volume fraction for the three high-pressure oxy-fuel turbulent methane jet flames at 1 bar, 3 bar, and 5 bar is shown in Fig. 3.

Fig. 3a) and b) show the composite image of the three flames' 2D instantaneous soot volume fraction distribution. Fig. 3a) shows the instantaneous image that deviates the most from the mean, while Fig. 3b) shows the image that is closest to it. For the 1 bar flame, soot appears in isolated patches and at relatively lower concentrations than the other flames. Moreover, soot pockets are visible at higher axial locations, suggesting a delayed onset of soot formation. As pressure (and Reynolds number) increases to 3 bar, soot filaments become finer and exist at considerably higher concentrations than the 1 bar flame. There is an approximately 3.5-fold increase in the maximum instantaneous soot volume fraction as the pressure is increased to 3 bar. Furthermore, it can also be observed that soot inception moves closer to the fuel tube as the pressure is tripled. At 5 bar, the instantaneous image reveals more complex and tightly packed structures that manifest at more upstream locations, suggesting earlier and more vigorous soot formation compared to the other two cases. In fact, the maximum instantaneous SVF increases by almost a factor of 6.6 when compared to the 1 bar case. The observations of soot behaviors with pressure align with previous studies indicating enhanced soot inception rates and particle growth at elevated pressures due to accelerated chemical kinetics and improved soot precursor formation pathways [22].

Fig. 3c) and d) show the time-averaged mean and RMS of the fluctuations of the flames. Both mean and RMS for all three flames tend to be roughly axisymmetric about the burner axis. As was observed in the instantaneous images, the mean soot level is highly sensitive to pressure. The maximum mean SVF rises by almost a factor of 7 as the pressure is raised to 3 bar and by a factor of 14 at 5 bar. The maximum mean SVF rises by almost a factor of 7 as the pressure is raised to 3 bar and by a factor of 14 at 5 bar. Previous work have described the pressure dependence of the peak SVF using a power law [15,19]. Assuming a power law behavior also for this class of oxy-fuel flames, we observe that the mean SVF scales as $P^{1.7}$. It is evident that the maximum mean SVF increases more rapidly with pressure than in the maximum instantaneous case. This difference comes about mainly because the averaging process does not take into account the intermittency difference between the flames. More discussion on intermittency will be provided in section 3.2. The RMS also shows that the largest temporal fluctuations happen around the same place in the central region where the mean peaks. Moreover, we see a consistently higher RMS than the mean for all the cases, indicating significant fluctuation of soot over time for all the cases. Notable RMS values are also observed near the edges, where the local equivalence ratio and temperature vary significantly. The width of the mean images broadens with pressure going from 1 bar to three bar to 5 bar. This shows that at increased Reynolds numbers and higher pressures, the enhanced turbulence-chemistry interaction leads to more

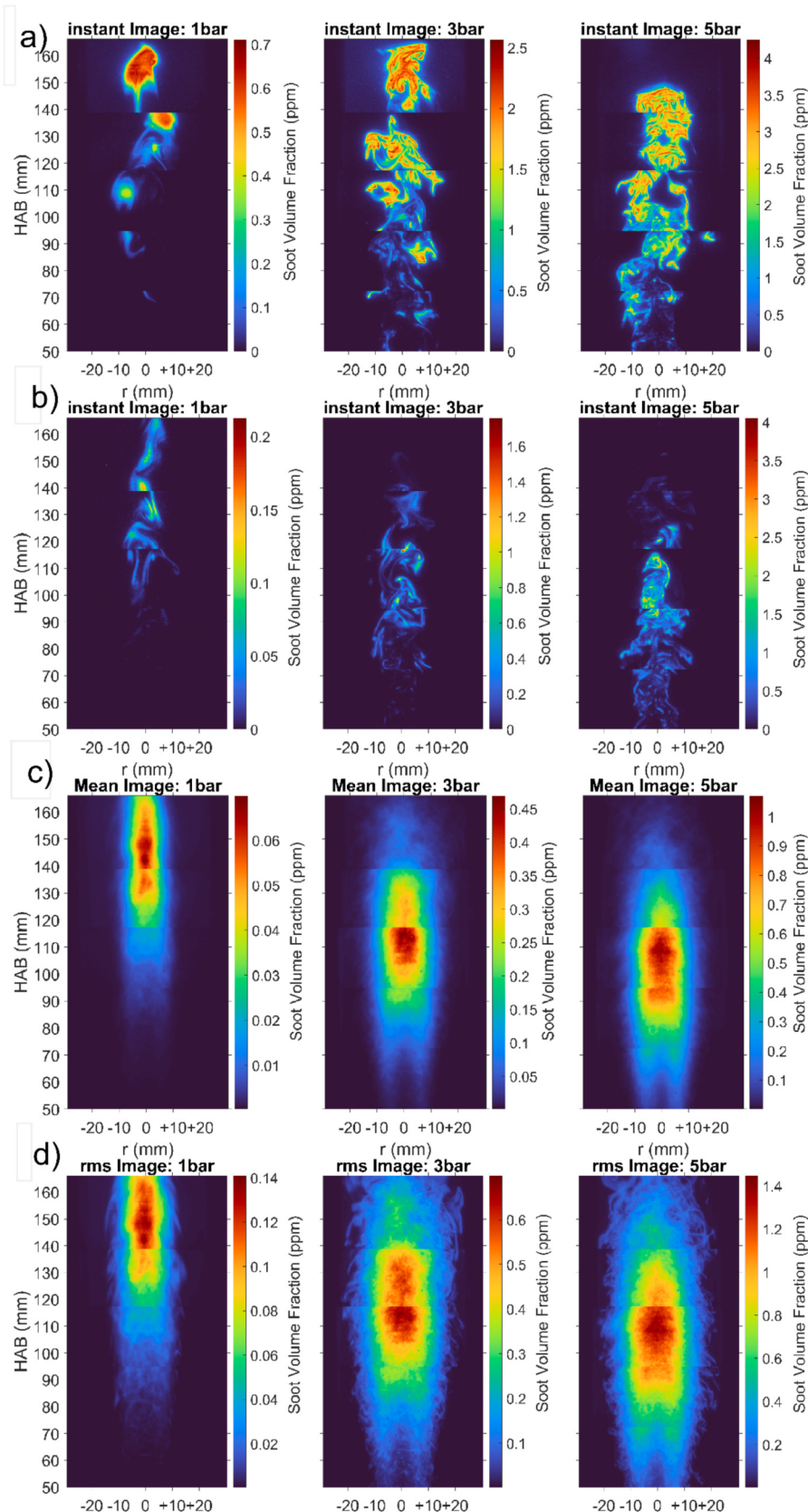


Fig. 3. 2D SVF distribution of a) instantaneous images (farthest from the mean), b) instantaneous images (closest to the mean), c) mean image, and d) RMS image. HAB (or x) stands for Height Above Burner. A separate scale was used for each case in order to enhance visualization for the 1-bar flame with low signal. Note: The upper section of the 1 bar flame is not shown here due to the limited range of the Z-translation stage, which prevented the laser sheet from illuminating the upper portions of the flame.

intense soot with high temporal and spatial variation.

3.2. Axial soot volume fraction distribution

Fig. 4 shows the centerline profiles of Mean, RMS, Intermittency, and RMS/Mean. The centerline data are plotted against axial height normalized by flame length (x/L_f) obtained from the DSLR images.

Fig. 4 a) presents the mean soot volume fraction distribution along the flame centerline. The centerline values were defined as the average intensity of the centerline pixel and the two pixels before and after. The scattered dots represent the experimental data, while the solid lines show the corresponding Gaussian fits. Following established practice in axisymmetric turbulent flame soot studies [12,17,31,32], Gaussian fitting is used to maintain consistency with previous measurements and to enable meaningful comparisons with our flame conditions. The 1 bar flame data is incomplete, as we could not sufficiently translate the burner inside our pressure vessel due to physical constraints. Hence, only data up to ~ 0.7 normalized height were obtained because the 1 bar flame is relatively taller than the other two, as seen in **Fig. 2**. **Fig. 4 a)** shows a general increase in SVF with pressure, with the peak increasing by a factor of 6.7 and 10, as the pressure is at 3 bar and 5 bar, respectively. Previous research [14] has indicated a small inverse dependence of centerline instantaneous SVF on Reynolds number; thus, the observed

SVF increase in our flames can be attributed mainly to the pressure effects. Interestingly, the peak in centerline mean SVF consistently occurred at a normalized height of $0.6 < x/L_f < 0.65$ for all three pressure/Reynolds number cases. This trend matches the observations of Mahmoud et al. [14] in atmospheric ethylene-air flames with Reynolds numbers of 5000, 8000, and 15,000, where the peak soot location also remained in the region $0.58 < x/L_f < 0.64$. Although their flames differ with ours in fuel type, oxidizer, and pressure, the agreement in normalized peak position suggests a level of insensitivity to Reynolds number, pressure, and fuel chemistry. This points to an underlying similarity in the large-scale structure of turbulent diffusion flames when viewed in normalized coordinates.

Fig. 4 b) shows the RMS fluctuations around the mean of all three cases examined in this study. Like the mean data, the RMS exhibits a near-Gaussian distribution to a high degree of accuracy, with scatter increasing with pressure. It can be seen that the Peak RMS is slightly downstream relative to the mean. Notably, our results show consistently higher RMS values the mean, implying greater temporal unsteadiness compared to a similar study by Boyette et al. [12] in high-pressure LII studies in ethylene-air flame.

To look into the fluctuations more in-depth, we plot the RMS/Mean ratio of the flames in **Fig. 4 c)**. The RMS/Mean ratio agreed well with a second-order Gaussian distribution for all the flames examined. We

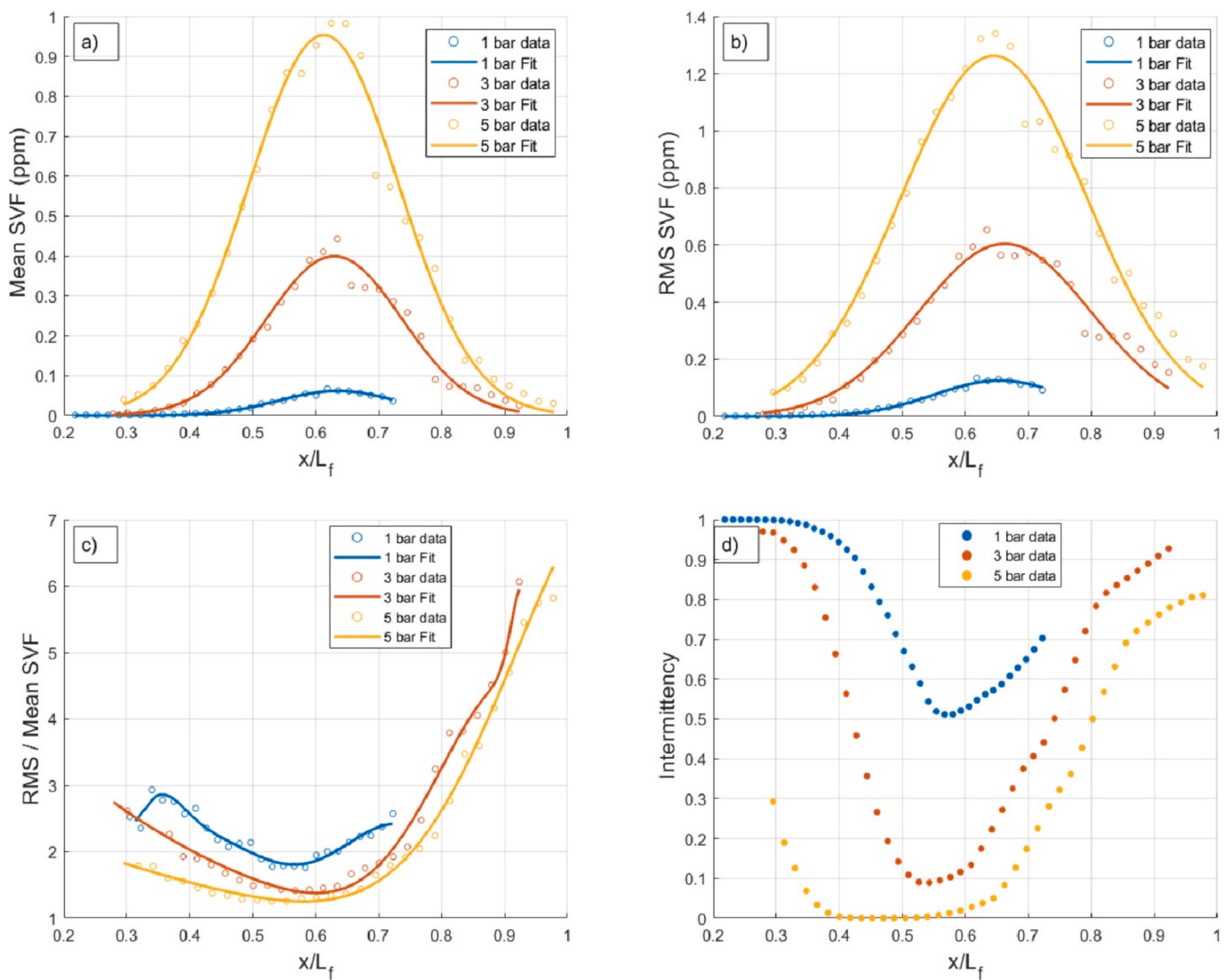


Fig. 4. Plot of a) mean b) RMS c) RMS/mean d) Intermittency for turbulent oxy-fuel flames plotted against normalized axial height (x/L_f).

notice that the 1 bar flames have the highest RMS/Mean ratio, indicating relatively larger temporal changes for these flames. We also notice that the RMS/mean curves tend to decrease as the pressure goes from 1 bar to 5 bar, with the minimums of the curves spatially aligning with the regions of least intermittency (see Fig. 4 d).

Fig. 4 d) shows the plot of axial intermittency against normalized axial height. Intermittency is defined [31,32] as the probability of soot absence at any given location along the centerline. Its value ranges from 0 (always soot) to 1 (no soot). For example, if intermittency is 0.4, soot is above the detection limit 60 % of the time. Because we are comparing Intermittencies across different pressures, we choose to apply a fixed cut-off threshold value (of 0.01 ppm) instead of the dynamic thresholding adopted in the study by Boyette et al. [12]. The plot shows intermittency decreases significantly as the pressure increases, particularly in the axial region $0.4 < x/L_f < 0.7$, reflecting a denser, more continuous soot field at higher pressures.

To better understand the observed trends in the mean and RMS SVF, we plot the normalized probability density function (P/P_{\max}) of instantaneous SVF at three locations along the centerline, (Fig. 5). The PDF plots were obtained for axial locations corresponding to $x/L_f = 0.4$ (soot formation region), $x/L_f = 0.55$ (peak soot region), and $x/L_f = 0.7$ soot oxidation region. The square dots shown on each curve signify the mean of the distribution. Note that the soot volume fraction (horizontal axis) is plotted on a logarithmic scale to allow for easier comparison between the three flames. As expected, the modal location of the PDF shifts to the right with increased pressure while the width of the PDF reduces. Hence, at high pressures, the SVF tends to converge on higher values and with less variability than the lower pressure cases, consistent with our Intermittency plots in Fig. 4. The shape of the 1 bar flame is roughly similar at all three axial heights the most probable value being zero ppm (no soot), suggesting high intermittency at all locations for the 1-bar case.

The shapes of the 3-bar and 5-bar flames' SVF distribution are approximately log-normal, with their peak lying to the left of the mean at $x/L_f = 0.4$. This behavior indicates that in the soot inception region, the dominant behavior is low-level soot formation with the occasional appearance of soot pockets with higher concentrations. A similar observation was made by Boyette et al. [12] in their study of 3-bar and 5-bar ethylene-air flames. The PDF shows a bi-modal peak with the mean lying between the two peaks in the peak soot region. The peaks and the mean of the SVF are higher than in the inception region, reflecting that the soot formation is at its maximum. At the onset of oxidation ($x/L_f = 0.7$), the soot distribution tends to move towards lower values even though many high soot occurrences exist, especially for the 5-bar flame. The above instantaneous analysis provides deeper insights into the spatial evolution of soot within these high-pressure turbulent flames. It is also clear that general quantities such as the mean/RMS are not sufficient to fully describe the effect of pressure (and Reynolds number) in these high-pressure turbulent flames [12].

3.3. Integrated SVF and global correlations

Fig. 6 presents the Radially Integrated SVF (SVF_{rad}) profiles obtained from the mean image. The definition of this quantity can be found in previous publications [24,32,33] and is given as:

$$SVF_{rad} = 2\pi \int_0^R f_v(r, h) r dr$$

where R stands for the distance from the centerline to the soot boundary on the laser-in side of the flame. To minimize the effect of noise, the soot boundary is set at 5 % of the maximum SVF value [24].

We observe that the SVF_{rad} profiles increase significantly as the pressure increases. Moreover, the location at which the peak of SVF_{rad} occurs corresponds to where the mean peaks, roughly between $0.6 < x/L_f < 0.65$. To account for the size and volume difference between the

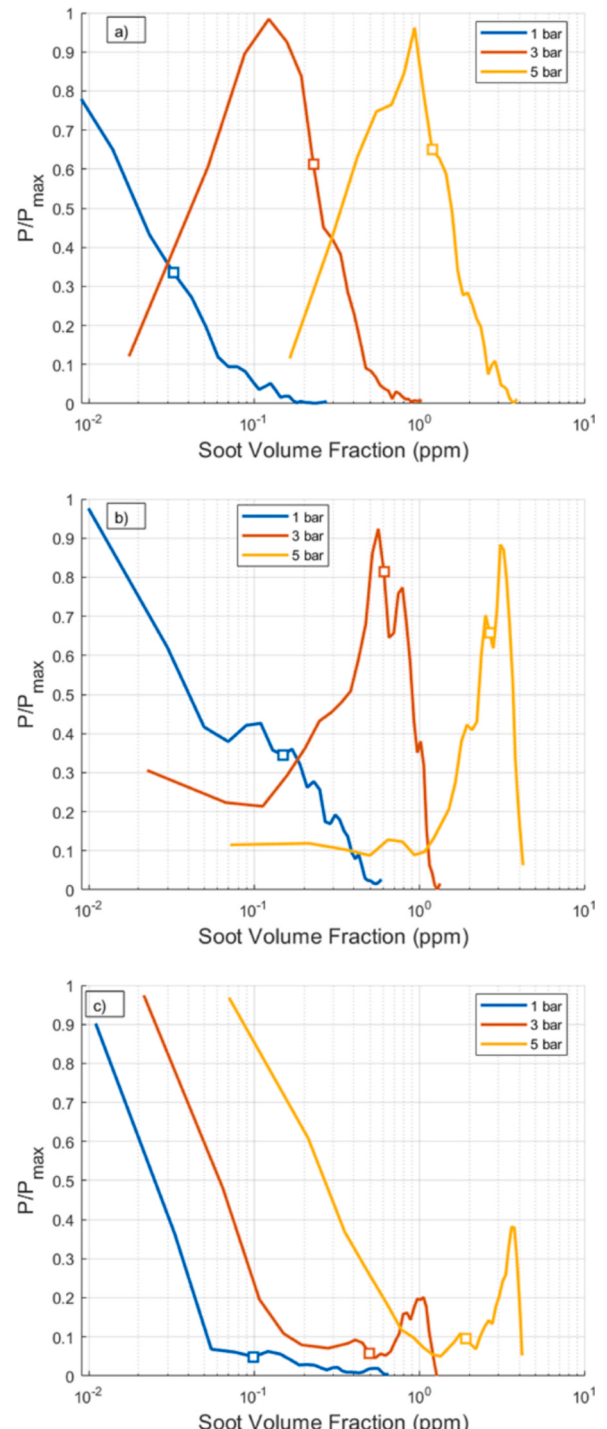


Fig. 5. Probability Density Function of the high-pressure oxy-fuel flames at a) normalized height of $x/L_f = 0.4$, b) normalized height $x/L_f = 0.55$, and c) normalized height $x/L_f = 0.7$.

flames, Fig. 7 shows volumetrically integrated SVF (SVF_{vol}) by integrating the SVF_{rad} along the non-normalized flame length [34,35]. As noted earlier, our 1-bar flame dataset extends only to about 0.7 normalized flame height, while SVF_{vol} requires full SVF_{rad} data. Because the observed SVF_{rad} profiles at 3 and 5 bar are symmetric, we assumed symmetry also for the 1 bar data to extrapolate the missing data. While this approach allowed us to estimate the missing portions, it introduces some uncertainty in SVF_{vol} values for 1 bar and consequently in the scaling as well.

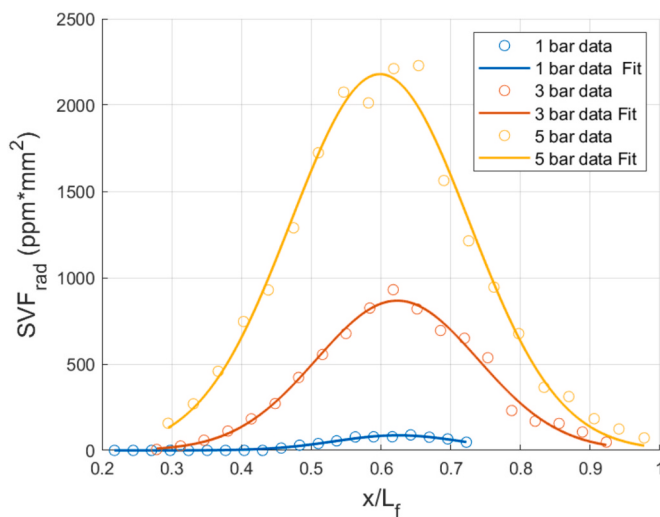


Fig. 6. Radially integrated SVF plotted against normalized heights for our three test cases. The solid lines are Gaussian fits to the data points represented by the unfilled circles.

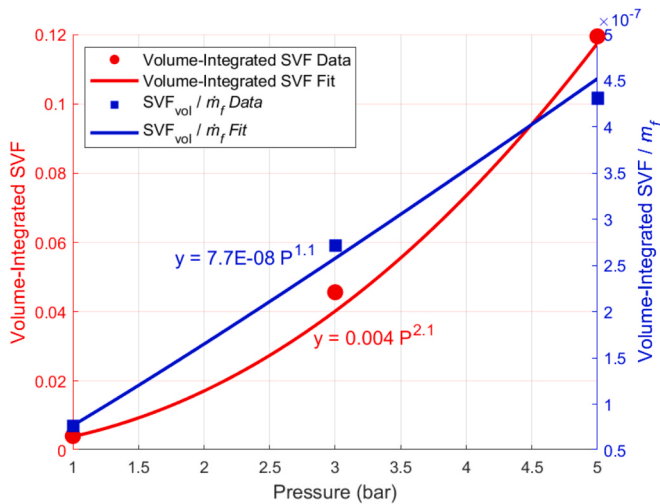


Fig. 7. Plot of volume-integrated SVF (red) and Volume-integrated SVF / fuel mass flow rate (blue) as a function of pressure. The squares and the circles represent data, while the solid lines are the power-law fits to the data. (For interpretation of the references to colour in this figure legend, the reader is referred to the web version of this article.)

The dependence of SVF_{vol} on pressure can be best characterized by a power law of approximately $P^{2.1}$. However, additional data points at intermediate and higher pressures would be essential to increase our confidence in this scaling. High-flow air cooling (>1000 SLM) is required to protect the BPR restricted stable operation to ~ 20 min, making further measurements impractical in the present configuration.

When pressure is increased at constant bulk jet velocity, the carbon flow rate also increases. Consequently, the observed $P^{2.1}$ is influenced not only by pressure but also by the additional carbon provided. To isolate the pressure effect, we also present the SVF_{vol} per the fuel flow rate as a function of pressure in Fig. 7 (in blue). After normalization, the dependence on pressure drops to approximately $P^{1.1}$. This suggests that the increased carbon input partly causes the previous scaling, and the intrinsic pressure effect on the total soot loading is more modest, scaling nearly linearly with pressure. This scaling is lower than the $P^{1.5}$ reported by Boyette et al. [12] for their high-pressure ethylene-air flame, perhaps due to the differences in fuel chemistry and temperature [36–38].

Additionally, CO₂ has been shown to oxidize soot at high temperatures and pressures through the reaction C + CO₂ → 2CO [39,40]. Therefore, the lower normalized scaling observed in our study may arise from both the fuel's carbon loading and the enhanced oxidative environment in O₂/CO₂ oxidizers.

4. Conclusion

This study provides a comprehensive experimental investigation into the effects of pressure on soot formation in turbulent oxy-fuel methane jet flames. DSLR images confirmed that increasing pressure leads to greater flame luminosity and reduced flame length due to increased density effects. Planar soot volume fraction distributions demonstrated a substantial rise in soot formation, with instantaneous SVF increasing by factors of 3.5 and 6.6 at 3 bar and 5 bar, respectively, relative to 1 bar. The mean SVF showed an even more pronounced rise, increasing by factors of 7 and 14 at 3 bar and 5 bar, respectively. Analysis of intermittency revealed a more continuous soot field at higher pressures, while PDF distributions indicated a shift toward higher soot concentrations and reduced fluctuations. The integrated SVF results confirmed a power-law scaling of total soot loading with pressure, with a dependence of $P^{2.1}$. However, normalizing by the fuel mass flow rate reduced the pressure dependence to $P^{1.1}$, suggesting that increased carbon input contributes significantly to the observed trends. These results underscore the importance of pressure in enhancing soot inception, growth, and oxidation dynamics in turbulent oxy-fuel flames. Future work should focus on exploring fuel composition effects and oxidation kinetics to further refine our understanding of soot formation mechanisms in high-pressure combustion environments.

CRediT authorship contribution statement

Muhammad Bukar: Writing – original draft, Visualization, Validation, Software, Methodology, Investigation, Formal analysis, Conceptualization. **Suman Basnet:** Writing – review & editing, Investigation. **Taesung Kim:** Writing – review & editing, Investigation. **William Roberts:** Supervision. **Gaetano Magnotti:** Writing – review & editing, Supervision, Resources, Funding acquisition.

Declaration of competing interest

The authors declare that they have no known competing financial interests or personal relationships that could have appeared to influence the work reported in this paper.

Acknowledgment

This work was funded entirely by the King Abdullah University of Science and Technology, Saudi Arabia, under CRG8 grant URF/1/4052-01-01.

Appendix A. Supplementary data

Supplementary data to this article can be found online at <https://doi.org/10.1016/j.fuel.2025.136895>.

Data availability

Data will be made available on request.

References

- [1] Selma L, Seigo O, Dohle S, Siegrist M. Public perception of carbon capture and storage (CCS): a review. Renew Sustain Energy Rev 2014;38:848–63.
- [2] Wall T, Liu Y, Spero C, Elliott L, Khare S, Rathnam R, et al. An overview on oxyfuel coal combustion—State of the art research and technology development. Chem Eng Res Des 2009;87:1003–16.

- [3] Barelli L, Bidini G, Gallorini F, Servili S. Hydrogen production through sorption-enhanced steam methane reforming and membrane technology: a review. *Energy* 2008;33:554–70.
- [4] Allam RJ, Palmer MR, Brown Jr GW, Fetvedt J, Freed D, Nomoto H, et al. High efficiency and low cost of electricity generation from fossil fuels while eliminating atmospheric emissions, including carbon dioxide. *Energy Procedia* 2013;37:1135–49.
- [5] Sammak M, Thern M, Genrup M. Performance of a semi-closed oxy-fuel combustion combined cycle (SCOC-CC) with an air separation unit (ASU). *Turbo Expo: Power for Land, Sea, and Air Am Soc Mech Eng* 2018;V003T06A10.
- [6] Allam R, Martin S, Forrest B, Fetvedt J, Lu X, Freed D, et al. Demonstration of the Allam Cycle: an update on the development status of a high efficiency supercritical carbon dioxide power process employing full carbon capture. *Energy Procedia* 2017;114:5948–66.
- [7] Dardi A, Prabhakar R, Tranier J-P, Perrin N. Air separation and flue gas compression and purification units for oxy-coal combustion systems. *Energy Procedia* 2009;1:527–34.
- [8] Andersson K, Johnsson F. Process evaluation of an 865 MWe lignite fired O₂/CO₂ power plant. *Energ Conver Manage* 2006;47:3487–98.
- [9] Kerr RA. Soot is warming the world even more than thought. *Am Assoc Advance Sci* 2013.
- [10] Lighty JS, Veranth JM, Sarofim AF. Combustion aerosols: factors governing their size and composition and implications to human health. *J Air Waste Manage Assoc* 2000;50:1565–618.
- [11] Kumfer B, Kennedy I. The role of soot in the health effects of inhaled airborne particles. Combustion generated fine carbonaceous particles. In: Proceedings of an International Workshop held in Villa Orlandi. Anacapri: Karlsruhe University Press; 2009. p. 1–15.
- [12] Boyette WR, Bennett AM, Cenker E, Guibert TF, Roberts WL. Effects of pressure on soot production in piloted turbulent non-premixed jet flames. *Combust Flame* 2021;227:271–82.
- [13] Bukar M, Basnet S, Wu B, Magnotti G. An experimental study of the stability and nearfield structure of oxyfuel jet flames at elevated pressures. *turbo expo: power for land, sea, and air. Am Soc Mech Eng* 2023;V03BT4A005.
- [14] Mahmoud S, Nathan G, Alwahabi Z, Sun Z, Medwell P, Dally B. The effect of exit Reynolds number on soot volume fraction in turbulent non-premixed jet flames. *Combust Flame* 2018;187:42–51.
- [15] Thomson KA, Gülder ÖL, Weckman EJ, Fraser RA, Smallwood GJ, Snelling DR. Soot concentration and temperature measurements in co-annular, nonpremixed CH₄/air laminar flames at pressures up to 4 MPa. *Combust Flame* 2005;140:222–32.
- [16] Lee W, Na YD. Soot study in laminar diffusion flames at elevated pressure using two-color pyrometry and Abel inversion. *JSME Int J, Ser B* 2000;43:550–5.
- [17] Flower W. Soot particle temperatures in axisymmetric laminar ethylene-air diffusion flames at pressures up to 0.7 MPa. *Combust Flame* 1989;77:279–93.
- [18] Flower W, Bowman C. Soot production in axisymmetric laminar diffusion flames at pressures from one to ten atmospheres. Symposium (International) on Combustion: Elsevier; 1988. p. 1115–24.
- [19] McCrain L, Roberts WL. Measurements of the soot volume field in laminar diffusion flames at elevated pressures. *Combust Flame* 2005;140:60–9.
- [20] Mandatori PM, Gülder ÖL. Soot formation in laminar ethane diffusion flames at pressures from 0.2 to 3.3 MPa. *Proc Combust Inst* 2011;33:577–84.
- [21] Flower W. An investigation of soot formation in axisymmetric turbulent diffusion flames at elevated pressure. Symposium (International) on Combustion: Elsevier; 1989. p. 425–35.
- [22] Fischer B, Moss J. The influence of pressure on soot production and radiation in turbulent kerosine spray flames. *Combust Sci Technol* 1998;138:43–61.
- [23] Wang H. 2nd International Sooting Flame Workshop in Livermore, CA on August 2–3, 2014. NSF Award Number 1445921 Directorate for Engineering. 2014;14:45921.
- [24] Bakar M, Basnet S, Liu P, Magnotti G. Effect of oxygen concentration and N₂-substitution on soot formation of a coflow oxy-fuel CH₄ laminar diffusion flames. *Fuel* 2025;386:134291.
- [25] Zhang Z, Zhou L, He X. Can laser-induced incandescence calibrated by laser extinction method be used for quantitative determination of soot volume fraction in laminar flames? *Appl Energy Combust Sci* 2023;13:100103.
- [26] Darabkhani HG, Zhang Y. Methane diffusion flame dynamics at elevated pressures. *Combust Sci Technol* 2010;182:231–51.
- [27] Kojima J, Ikeda Y, Nakajima T. Basic aspects of OH (a), CH (a), and C₂ (d) chemiluminescence in the reaction zone of laminar methane-air premixed flames. *Combust Flame* 2005;140:34–45.
- [28] Karnani S, Dunn-Rankin D. Visualizing CH* chemiluminescence in sooting flames. *Combust Flame* 2013;160:2275–8.
- [29] Delichatsios M. Transition from momentum to buoyancy-controlled turbulent jet diffusion flames and flame height relationships. *Combust Flame* 1993;92:349–64.
- [30] Guibert TF, Boyette WR, Roberts WL. Height of turbulent non-premixed jet flames at elevated pressure. *Combust Flame* 2020;220:407–9.
- [31] Qamar N, Nathan G, Alwahabi Z, King K. The effect of global mixing on soot volume fraction: measurements in simple jet, precessing jet, and bluff body flames. *Proc Combust Inst* 2005;30:1493–500.
- [32] Mahmoud S, Nathan G, Alwahabi Z, Sun Z, Medwell P, Dally B. The effect of exit strain rate on soot volume fraction in turbulent non-premixed jet flames. *Proc Combust Inst* 2017;36:889–97.
- [33] Sun Z, Dally B, Alwahabi Z, Nathan G. The effect of oxygen concentration in the co-flow of laminar ethylene diffusion flames. *Combust Flame* 2020;211:96–111.
- [34] Zelepouga SA, Saveliev AV, Kennedy LA, Fridman AA. Relative effect of acetylene and PAHs addition on soot formation in laminar diffusion flames of methane with oxygen and oxygen-enriched air. *Combust Flame* 2000;122:76–89.
- [35] Zhang Z, Zhang C, Wu Y, Zhang J, He X, Zhou L. Effects of N₂ and CO₂ addition to oxidizer on soot formation in n-heptane laminar diffusion flame at preheating temperatures. *Fuel* 2024;374:132480.
- [36] Bockhorn H. Soot formation and oxidation. *Pollutants from Combustion: Formation and Impact on Atmospheric Chemistry*: Springer; 2000. p. 205–39.
- [37] Haynes BS, Wagner HG. Soot formation. *Prog Energy Combust Sci* 1981;7:229–73.
- [38] Wagner HG. Soot formation—an overview. *Particulate Carbon: Formation During Combustion*. 1981:1–29.
- [39] Zhang S, Wang M, Liang C, Zhu Z. Experimental study on the improvement of char physicochemical properties and reactivity by activation process in CFB. *ACS Omega* 2024;9:24500–12.
- [40] Mianowski A, Robak Z, Tomaszwicz M, Stelmach S. The Boudouard–Bell reaction analysis under high pressure conditions. *J Therm Anal Calorim* 2012;110:93–102.